Development of a 7-DoF Haptic Operator Interface Based on Redundantly Actuated Parallel Mechanism

Jichen Li, Ziyan Huang, Chengzhi Hu, Zhiqiang Zhang, Chaoyang Shi*

Abstract—**This paper proposes a novel 7-DoF operator interface based on a redundantly actuated parallel architecture of 2(RRRS)-RRRSP. This design effectively avoids the workspace-internal singularities, thereby addressing the limitations associated with the orientational workspace of traditional parallel operator interfaces. Furthermore, the redundantly actuated mechanism enables 3-DoF full actuation of each branch chain, and the motors are specially positioned near the base, significantly reducing the operating inertia without the need for gravity compensation. This arrangement contributes to a reduction in operator fatigue during prolonged operation. A hybrid tendon-linkage transmission is utilized in the operator interface to enhance its positioning accuracy. A prototype of the operator interface has been developed, and its kinematics, along with the Jacobian, have been derived. Optimization of structural parameters has been executed to enhance operational dexterity and relative workspace. Static force analysis has been conducted, and a strategy for static force output has been implemented to effectively decouple the interference between the clamping feedback force and the six-dimensional spatial feedback force. Experimental investigations on the translational and orientational workspace are carried out. The results demonstrate an expansive translational workspace measuring 315 mm (X), 248.5 mm, and 133.8 mm (Z), along with a wide range of orientation angles [-108°, 98°] (α), [-134°, 134°] (β) and [-115°, 115°] (γ). Trajectory tracking experiments have been performed and yielded an average error value of 1.021mm. The accuracy of the feedback force output has been studied, with average errors in output force recorded as 0.084 N (X), 0.124 N (Y), and 0.237 N (Z). Investigations into decoupling capability have been carried out, with average output errors of the clamping force at 5 N and 7 N operating forces in X and Y directions recorded as 0.095 N and 0.081 N, respectively. The experimental results demonstrate its potential for integration into RAMIS systems to align with diverse configurations of slave manipulators.**

Index Terms— **Operator interface, haptic device, parallel mechanism, design optimization, robot-assisted minimally invasive surgery.**

I. INTRODUCTION

Robot-assisted minimally invasive surgery (RAMIS) is a clinical approach that amalgamates advanced robotic technology, real-time imaging, and human-machine interaction [1-3], which has achieved global adoption in recent years. RAMIS offers many benefits, including precise positioning, improved dexterity, high-resolution video stream, and effective human-machine interaction[4-9]. These advantages contribute to reducing physician fatigue and errors during procedures, thereby leading to a decreased risk of infection, expedited recovery, and heightened patient satisfaction [10-13]. The RAMIS system typically comprises a master console and a slave manipulator. The operator interface serves as the critical role of the master console between the surgeons and the slave manipulator, responsible for transmitting control commands to the robotically articulated instruments and receiving haptic feedback [14-16]. The surgeon manipulates surgical instruments through the master console, resulting in a loss of direct tactile perception of the organ or tissue. Therefore, haptic feedback of the operational interface plays a crucial role in facilitating an accurate assessment of surgical outcomes by enhancing the surgeon's perception of the target area. Consequently, the design and performance of the operator interface significantly impact the effectiveness of RAMIS in enhancing the surgeon's ability to perceive the state of the target area and surgical outcomes.

In recent years, several operator interfaces have been developed and can be broadly categorized into two types based on their structures: serial operator interfaces and parallel operator interfaces. The serial operator interfaces include the 8-DoF serial interface that is commercially available and is equipped in the da Vinci system by Intuitive Surgical Inc [17], [18]. The joint axes of the wrist part intersect at a single point, ensuring flexible and independent adjustment of the operator interface's orientation. Sang et al. developed a serial 6-DoF operator interface [19], integrated into the MicroHand robot system, which achieves decoupling between position and orientation. Liang et al. designed a 9-DoF operator interface [20] incorporating a redundant position compensation mechanism to achieve decoupling between the position and orientation in the grasping point. France et al. have developed a 4-DoF operator interface integrated into the K-Flex system for NOTES procedures [21]. This device features an isomorphic structure, exhibiting a DoF arrangement that closely mirrors that of the slave manipulators. The commercial PHANTOM devices [22] developed by Sensable offer 6-DoF motion and 3D force feedback. This device features a compact structure that facilitates precise positioning input and delivers high-fidelity

force feedback output. In addition, it has been successfully integrated into various industries, including digital entertainment games, virtual reality, remote operation, and other related fields. The serial operator interface features a simple structure and an expanded workspace. However, there are still problems such as low stiffness and diminished precision. Additionally, the elongated linkages require high joint torque and a large reduction ratio gear mechanism, increasing friction torque in the active joint and impacting operational compliance.

Several parallel operator interfaces have been developed, which can effectively solve the above problems. Daekeun Ji et al. designed a 3-DoF operator interface [23], which utilizes a variable isosceles triangle mechanism to restrict the bending angle of the slave continuum manipulator, thereby controlling the tension in the cables within a safe range. However, this device offers limited DoF and poor ergonomics, restricting its applicability in other domains. Minh Hung Vu et al. have developed a 6-DoF parallel operator interface [24], which consists of two interconnected 3-DoF parallel structures and a steering handle, providing a 5-DoF spital and a 1-DoF twist motion. This design satisfies the requirements of low inertia and high output torques, but it exhibits limited orientation angles of ±90° about the X-axis and Y-axis. A series of haptic devices designed by the Swiss company Force Dimension have successfully been designed and commercialized. The Omega.3 operator interface is developed with a classic delta parallel structure that provides 3-DoF motion and enhances overall stiffness [25]. With an output force capability of up to 12 N, it enables three-dimensional force feedback at the distal end effector. Omega.7 [26] was developed by adding a 3 DoFs concurrent mechanism to the Omega.3, providing motion and an additional gripping DoF. The translational and gripping DoFs are actuated to provide force feedback, while each rotational DoF is equipped with an encoder only and cannot output force. Sigma.7 [27] was developed to further upgrade the force output capability of Omega.7, and all its joints are equipped with servomotors, allowing 6D spatial feedback force. It has large force feedback and can provide fast and precise force interaction. However, this device incorporates a sophisticated distal orientational and clamping structure with significant inertia, resulting in the reliance on gravity compensation algorithms and diminished dynamics.

In a typical RAMIS process, the intuitive and safety requirements prohibit the angular scaling between the orientation of the operator interface and the slave end-effector [28-30]. Therefore, it is necessary to design the operator interface with the most significant possible access angle to enhance the working range of the entire surgical robotic system. Additionally, the inclusion of clamping DoF and force feedback in the operator interface is imperative. A commonly employed solution involves incorporating an actuator into the handle of the operator interface, thereby increasing operational inertia and fatigue in long-term surgery. In summary, the existing parallel haptic devices need to enhance their adaptability to RAMIS by addressing the issues of limited orientational workspace and high operational inertia.

Extensive research has been conducted on the singularity avoidance capability of the redundantly actuated parallel mechanism [31]. The rationale can be qualitatively explained by referring to the Jacobian matrix. The condition for a type II (parallel) singularity is that this matrix becomes rank deficient. Generally, the Jacobian matrix of a non-redundant structure has equal rows and columns, with each row corresponding to a DoF of the mechanism. Introducing redundantly actuated DoFs increases the number of rows, resulting in more rows than columns in this matrix. Therefore, rank deficiency imposes a more stringent constraint compared with non-redundant robots, and achieving the geometric condition for parallel singularity becomes more challenging. Consequently, kinematic singularities can be minimized by introducing kinematic redundancy during the design stage.

To address the limited orientational workspace of traditional haptic devices and further minimize the operational inertia. A redundantly actuated operator interface is proposed to alleviate singularity issues and expand the orientational workspace. Additionally, the proposed device incorporates a specially designed motor arrangement and transmission mode to further reduce operational inertia and fatigue. The remaining sections of this paper are structured as follows. Section II provides a comprehensive explanation of the proposed redundantly actuated operator interface, including the design concept, system descriptions, kinematics, and Jacobian analysis, as well as the program for structural optimization. Experimental characterizations and hardware configuration are presented in Section III. Discussions are elaborated upon in Section IV with the conclusions summarized in Section V.

II. METHODS AND MATERIALS

A. Design of the Redundantly Actuated Parallel Operator Interface

The proposed haptic operator interface has been designed based on a redundantly actuated parallel mechanism, enabling translational, rotational, and grasping capabilities, as illustrated in Fig. 1a). This operator interface consists of a mobile plate connected to a horizontal base by three branch chains, which are then secured to a "L" shape fixed support. The three branch chains are redundantly actuated and distributed at an equal interval of 120°. The architecture of the operator interface can be described as 2(<u>R</u>RRS)-<u>R</u>RRSP, as shown in Fig. 2a). Here, <u>R</u> denotes the active revolute joints, which means that the mechanism is driven by nine motors in the driving space. The operational space of this mechanism enables 7-DoF movements, including 3-DoF translational and 3-DoF rotational movements and a 1-DoF clamming movement. Moreover, this device provides decoupled 6-DoF spatial feedback forces and the 1-DoF clamping feedback force to fulfill the interaction requirements in the RMIS process.

The detailed structural design of the branch chain is illustrated in Fig. 1b), comprising three motors, two pairs of capstans, a transmission linkage, a parallelogram structure, and
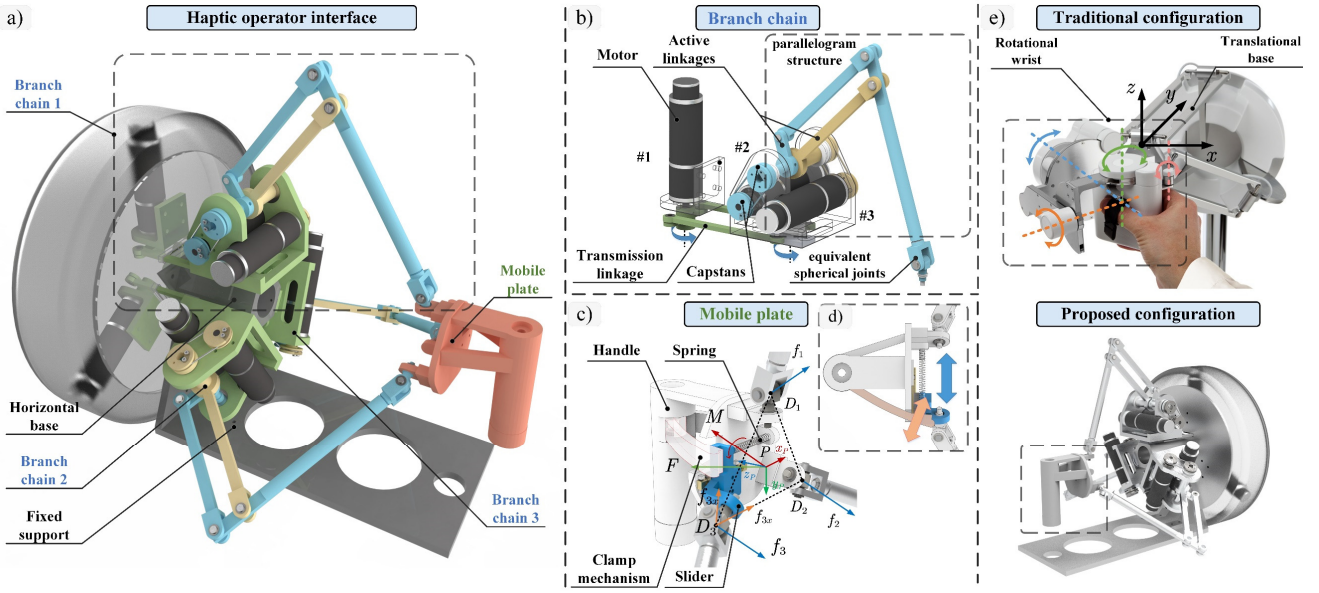
Fig. 1. a) Main components of the haptic operator interface. b) The detailed structural design of the branch chain. c) Detailed structure and schematic diagram of static force analysis for the mobile platform. d) The principle of the sliding DoF. e) The comparison between the traditional configuration (Sigma.7) and the proposed modified configuration of the operator interface.

an equivalent spherical joint. Two distinct transmission modes are employed in the branch chain. Considering the high requirement for accuracy, a linkage transmission is employed that the parallel transmission linkages are driven by motor #1 fixed on the base to rotate the entire branch chain. Compared to traditional belt or gear transmission, this method eliminates the need for a tensioning device and minimizes clearance-induced errors, rendering it suitable for this high-precision and small-range scenario. The two active linkages are driven by motors #2 and #3 through tendons and capstans in a 1:1 transmission ratio. Compared with direct transmission through couplings, this method allows for the motors' positioning near the self-rotation axis of the branch chain. Therefore, the rotational inertia of the branch chain is reduced, and the enhanced structural compactness minimizes internal interference, thereby improving the workspace of the entire mechanism. An equivalent spherical joint is designed at the end of the branch chain to achieve a 3-DoF motion, providing a wider rotation range than traditional spherical joints while overcoming issues related to waterproofing, dustproofing, and lubrication. The design of the mobile plate is illustrated in Fig. 1c), which mainly includes a handle, a clamp mechanism, a slider, and a reset spring. This structure serves as an interactive interface, providing an ergonomic grip for the operator while capturing the motion trajectory. The operator grasps the handle of the operator interface with their palm to receive a six-dimensional spatial feedback force. The principle of the sliding DoF is illustrated in Fig. 1d). The end joint of the branch chain is connected to the mobile plate through a slider, which restricts their relative linear displacement. During operation, the operator positions the index finger on the clamp mechanism to bear a one-dimensional clamping feedback force. The clamp mechanism always remains tangential to the slider due to the resetting spring with both ends fixed to the slider and handle

base. Notably, this spring has low stiffness to minimize interference with feedback clamping force.

The comparison between the traditional configuration (Sigma.7) and the proposed modified configuration of the operator interface is shown in Fig. 1e). The Sigma.7 utilizes a 3-DoF "delta" parallel structure as the translational base and the corresponding three driving motors are mounted on the base to lower the operating inertia. The rotational wrist extension is mounted on the output of the translational base and features a 3-DOF serial kinematics structure with three rotational joints arranged along intersecting axes. The grasping unit, positioned on the output of the wrist extension, comprises a fixed hand grip and a movable finger interface. However, the four motors for the 3-DOF serial joints and the grasping joint are embedded with them. Thus, this configuration exhibits significant operating inertia and necessitates precise gravity compensation, since the sophisticated layout of the rotational wrist is fully supported by the translational base. Compared with this traditional configuration, the proposed operator interface designs offer the following advantages. Firstly, the parallel mechanism is specially designed to reduce workspace-interior singularities, thereby significantly expanding the orientation workspace. The first joint of each branch chain is designed in the XY plane to avoid type I (serial) singularities, that is, the spherical joint D_i located on the axis of the first revolute joint. The type II (parallel) singularities are avoided by redundantly actuated DoF [32-34]. Secondly, the near-base driving of the orientation and clamping motion is achieved by utilizing three redundant branch chains to reconstruct the mobile plate's shape. It effectively reduces the operating inertia and fatigue from long-term operation without necessitating gravity compensation. Thirdly, the integration of wire and linkage transmissions improves structural compactness and minimizes backlash, effectively enhancing positioning accuracy.
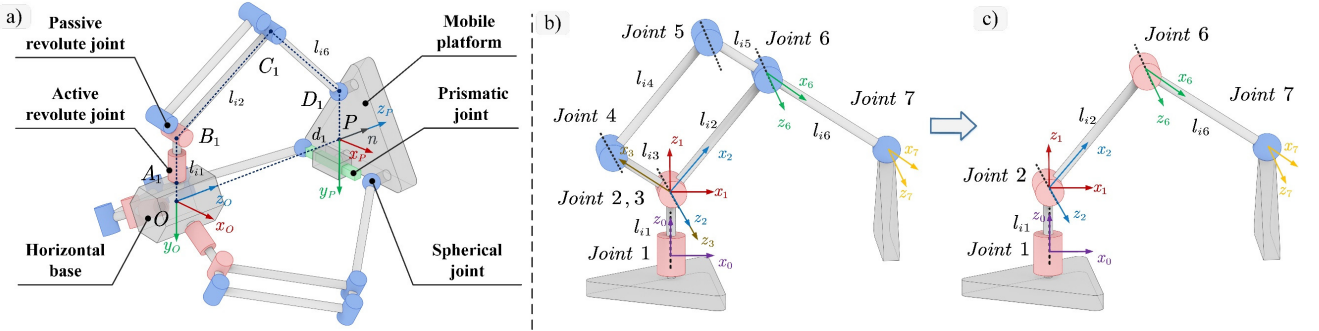
Fig. 2. a) Kinematic model of the redundantly actuated parallel operator interface. Here the red and blue cylinders represent active and passive joints, respectively. b) The architecture of the branch chain. c) The architecture of the equivalent serial branch chain.

B. Kinematics and Jacobian Analysis

1) kinematics of the operator interface

The forward and inverse kinematics of the operator interface are derived, and the associated terms and frames have been defined as shown in Fig. 2a). The base frame {O} is fixed to the base center, while the end effector frame {P} is fixed to the center of the mobile plate. A_i, B_i, C_i, and D_i represent the nodes of the links on the ith branch chain, l_{ij} (i=1, 2, 3; j =1, 2, 3, 4, 5, 6, 7;) denote the length of the jth link on each branch chain. All passive revolute joint axes are parallel to each other and oriented perpendicular to the axis of the active revolute joint, as shown in Fig. 2b). The initial length values of each link in the branch chain are enumerated in Table I.

TABLE I
INITIAL DESIGN PARAMETERS OF THE BRANCH CHAIN

Joint	Length of link
l_{i1}	107mm
l_{i2}	100mm
l_{i3}	25mm
l_{i4}	110mm
l_{i5}	25mm
l_{i6}	100mm

Since the branch chain adopts a parallelogram structure, it can be equivalent to a serial <u>RRRS</u> structure composed of Joints 1, 2, 6, and 7 to simplify the analysis. There are two actuated joints in Point B_i, which are driven by two motors. The rotation angles of motors #2 and #3 are denoted as θ_{i2} and θ_{i3}, respectively. The joint 6 is considered an active joint, and its equivalent rotation angle θ_{i6} can be calculated as:

$$\theta_{i6} = \theta_{i3} - \theta_{i2} + \pi. \tag{1}$$

The D-H parameters of the equivalent serial chain have been listed in Table II. The kinematics of the equivalent serial chain can be expressed as:

$$^0_7T = {}^0_1T{}^1_2T{}^2_6T{}^6_7T = \begin{bmatrix} {}^0_7R & {}^0_7p \\ \mathbf{0}_{1\times3} & 1 \end{bmatrix}, \tag{2}$$

TABLE II
D-H PARAMETERS OF THE EQUIVALENT SERIES BRANCH CHAIN

Index i	α_{i-1}	a_{i-1}	d_i	θ_i
1	0	0	l_{i1}	θ_1
2	90°	0	0	θ_2
6	0	l_{i2}	0	θ_6
7	0	l_{i6}	0	0

where ^0_7p denotes the position of Point D_i in frame {0}. ^j_iT

represents homogeneous transformation that relates frame {i} to frame {j} and it can be calculated as:

$$^{i-1}_iT = R_X(\alpha_{i-1})D_X(a_{i-1})R_Z(\theta_i)D_Z(d_i). \tag{3}$$

By substituting the known parameters of θ_{i1}, θ_{i2}, θ_{i6}, the position of Point D_i in frame {0}, $^{A_i}_{D_i}p$ can be obtained as

$$^{A_i}_{D_i}p = \begin{bmatrix} l_{i2}c_{\theta_{i1}}c_{\theta_{i2}} + l_{i6}(c_{\theta_{i1}}c_{\theta_{i2}}c_{\theta_{i6}} - c_{\theta_{i1}}s_{\theta_{i2}}s_{\theta_{i6}}) \\ l_{i2}s_{\theta_{i1}}c_{\theta_{i2}} + l_{i6}(s_{\theta_{i1}}c_{\theta_{i2}}c_{\theta_{i6}} - s_{\theta_{i1}}s_{\theta_{i2}}s_{\theta_{i6}}) \\ l_{i2}s_{\theta_{i2}} + l_{i6}(s_{\theta_{i2}}c_{\theta_{i6}} + c_{\theta_{i2}}s_{\theta_{i6}}) + l_{i1} \end{bmatrix}. \tag{4}$$

Therefore, the position of Point D_i in base frame {O} can be calculated as:

$$^O_{D_i}p = {}^O_{A_i}p + {}^O_{A_i}R\,^{A_i}_{D_i}p, \tag{5}$$

where $^O_{A_i}p$ and $^O_{A_i}R$ can be obtained by the geometric relationship of Points A_i and O.

The position of Point D_i in base frame {O} can alternatively be represented as:

$$^O_{D_i}p = {}^O_Pp + {}^O_PR\,^P_{D_i}p, \tag{6}$$

where $^P_{D_i}p$ denotes the position of D_i in frame {P}, which can be written as below:

$$^P_{D_i}p = \begin{cases} ^P_{D_1}p = [0 & y_1 & 0]^T \\ ^P_{D_2}p = [x_2 & y_2 & 0]^T \\ ^P_{D_3}p = [X_3 & y_3 & 0]^T \end{cases}, \tag{7}$$

where the constant values x_i and y_i can be obtained according to the geometric relationship, $X_3 = x_3 + d$ denotes the relevant position of Point D_3 to Point P in the x direction, and d represents the clamping distance of the mobile plate.

By combining Equations (1)-(7), the position ^O_Pp, orientation ^O_PR and clamping distance d can be derived. The inverse kinematics of the operator interface can be derived as follows. Considering the mobile plate position ^O_Pp, orientation ^O_PR, and clamping distance d, the position of Point D_i in frame {P} $^P_{D_i}p$ is determined by equations (6-7). The joint angles θ_{i1}, θ_{i2}, θ_{i3} can be obtained by substituting the results above into Equations (4), (5), and (1).

2) Jacobian Analysis of the Operator Interface

The Jacobian analysis of the proposed operator interface is performed, with the exclusion of the clamming DoF for simplifying calculations. Concerning Fig. 1d) for each loop A_i, B_i, C_i, D_i, and P in different legs, the following vector equation can be written as:

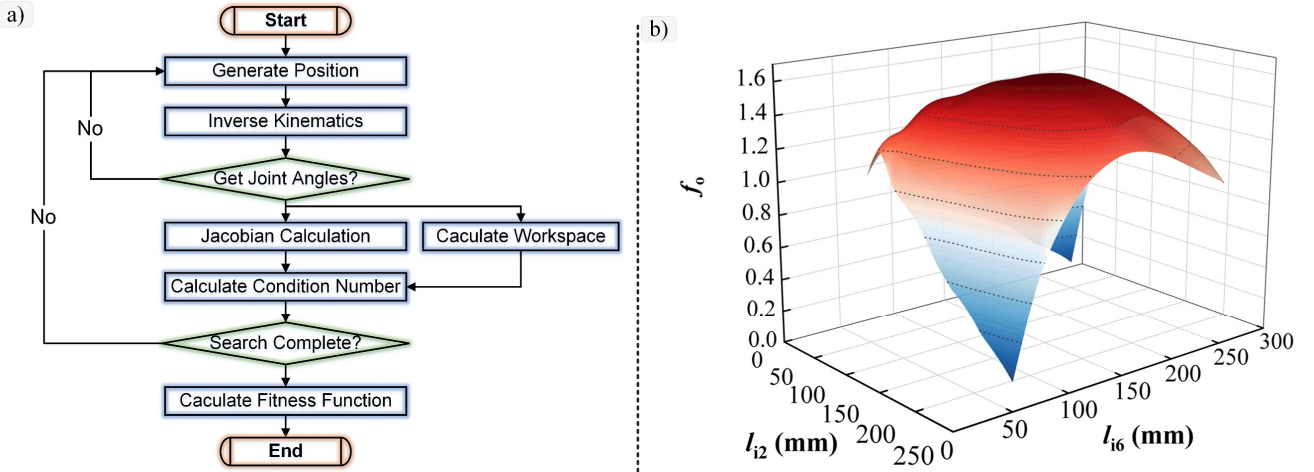$$^O_{A_i}p + l_{i1} + l_{i2} + l_{i6} = {}^O_Pp + {}^Od_i, \tag{8}$$

Fig. 3. a) Schematic diagram of the fitness function calculation workflow. b) Optimization results for different link length values.

where ${}^{O}_{A_i}\boldsymbol{p}$ and ${}^{O}_{P}\boldsymbol{p}$ denotes the position of the Point A_i and P in frame $\{O\}$, respectively. ${}^{O}\boldsymbol{d_i}$ denotes the position vector of P to D_i in frame $\{O\}$. By dividing both sides of this equation by the differential time element, it can be formulated as:

$$\boldsymbol{w}_{i1} \times (\boldsymbol{l}_{i2} + \boldsymbol{l}_{i6}) + \boldsymbol{w}_{i2} \times (\boldsymbol{l}_{i2} + \boldsymbol{l}_{i6}) + \boldsymbol{w}_{i6} \times \boldsymbol{l}_{i6}$$
$$= {}^{O}_{P}\boldsymbol{v} + {}^{O}_{P}\boldsymbol{w} \times {}^{O}\boldsymbol{d_i}, \quad (9)$$

where ${}^{O}_{P}\boldsymbol{v} = [x_P, y_P, z_P]^T$ represents the velocity vector of Point P, and ${}^{O}_{P}\boldsymbol{w}$ denotes the angular velocity vector of the mobile plate. Dotting both sides of Equation (9) with vector $\boldsymbol{n}, \boldsymbol{l}_{i2}$, and $\boldsymbol{l}_{i6}$ yields this result:

$$[(\boldsymbol{l}_{i2} + \boldsymbol{l}_{i6}) \times \boldsymbol{n}]w_{i1} + [(\boldsymbol{l}_{i2} + \boldsymbol{l}_{i6}) \times \boldsymbol{n}]w_{i2} + (\boldsymbol{l}_{i6} \times \boldsymbol{n})w_{i6}$$
$$= \boldsymbol{n} \cdot {}^{O}_{P}\boldsymbol{v} + ({}^{O}\boldsymbol{d_i} \times \boldsymbol{n}) \cdot {}^{O}_{P}\boldsymbol{w}, \quad (10)$$

$$(\boldsymbol{l}_{i6} \times \boldsymbol{l}_{i2})w_{i1} + (\boldsymbol{l}_{i6} \times \boldsymbol{l}_{i2})w_{i2} + (\boldsymbol{l}_{i6} \times \boldsymbol{l}_{i2})w_{i6}$$
$$= \boldsymbol{l}_{i2} \cdot {}^{O}_{P}\boldsymbol{v} + ({}^{O}\boldsymbol{d_i} \times \boldsymbol{l}_{i2}) \cdot {}^{O}_{P}\boldsymbol{w}, \quad (11)$$

$$(\boldsymbol{l}_{i2} \times \boldsymbol{l}_{i6})w_{i1} + (\boldsymbol{l}_{i2} \times \boldsymbol{l}_{i6})w_{i6}$$
$$= \boldsymbol{l}_{i6} \cdot {}^{O}_{P}\boldsymbol{v} + ({}^{O}\boldsymbol{d_i} \times \boldsymbol{l}_{i6}) \cdot {}^{O}_{P}\boldsymbol{w}, \quad (12)$$

where $\boldsymbol{n}$ denotes the normal vector of the unit mobile plate. $\boldsymbol{w}_{i1} = {}^{O}_{1}\boldsymbol{R}_i \boldsymbol{k}\dot{\theta}_{i1}, \boldsymbol{w}_{i2} = {}^{O}_{2}\boldsymbol{R}_i \boldsymbol{k}\dot{\theta}_{i2}, \boldsymbol{w}_{i6} = {}^{O}_{6}\boldsymbol{R}_i \boldsymbol{k}(\dot{\theta}_{i3} - \dot{\theta}_{i2}), \boldsymbol{k} = [0; 0; 1]^T$. Combining equations (10-12) and rearranging them in matrix form, the velocity equation can be obtained as

$$\boldsymbol{K_a}\dot{\boldsymbol{\theta}} = \boldsymbol{J_a}\dot{\boldsymbol{\chi}}, \quad (13)$$

where $\boldsymbol{K_a}$ and $\boldsymbol{J_a}$ are respectively 9×9 and 9×6 Jacobian matrices and the vector $\dot{\boldsymbol{\theta}}$ represents the angular velocities of the 9 active joints. The vector $\dot{\boldsymbol{\chi}} = [{}^{O}_{P}\boldsymbol{v}^T \; {}^{O}_{P}\boldsymbol{w}^T]$ denotes the Cartesian velocities of the mobile plate, and the form of the matrices $\boldsymbol{K}$ and $\boldsymbol{J}$ can be expressed as:

$$\boldsymbol{K_a} = \begin{bmatrix} K_{11} & K_{12} & K_{13} & 0 & 0 & 0 & 0 & 0 & 0 \\ K_{21} & K_{22} & K_{23} & 0 & 0 & 0 & 0 & 0 & 0 \\ K_{31} & K_{32} & 0 & 0 & 0 & 0 & 0 & 0 & 0 \\ 0 & 0 & 0 & K_{44} & K_{45} & K_{46} & 0 & 0 & 0 \\ 0 & 0 & 0 & K_{54} & K_{55} & K_{56} & 0 & 0 & 0 \\ 0 & 0 & 0 & K_{64} & K_{65} & 0 & 0 & 0 & 0 \\ 0 & 0 & 0 & 0 & 0 & 0 & K_{77} & K_{78} & K_{79} \\ 0 & 0 & 0 & 0 & 0 & 0 & K_{87} & K_{88} & K_{89} \\ 0 & 0 & 0 & 0 & 0 & 0 & K_{97} & K_{98} & 0 \end{bmatrix}, \quad (14)$$

$$\boldsymbol{J_a} = \begin{bmatrix} \boldsymbol{n}^T & ({}^{O}\boldsymbol{d_1} \times \boldsymbol{n})^T \\ \boldsymbol{l}_{12} & ({}^{O}\boldsymbol{d_1} \times \boldsymbol{l}_{12})^T \\ \boldsymbol{l}_{16} & ({}^{O}\boldsymbol{d_1} \times \boldsymbol{l}_{16})^T \\ \boldsymbol{n}^T & ({}^{O}\boldsymbol{d_2} \times \boldsymbol{n})^T \\ \boldsymbol{l}_{22} & ({}^{O}\boldsymbol{d_2} \times \boldsymbol{l}_{22})^T \\ \boldsymbol{l}_{26} & ({}^{O}\boldsymbol{d_2} \times \boldsymbol{l}_{23})^T \\ \boldsymbol{n}^T & ({}^{O}\boldsymbol{d_3} \times \boldsymbol{n})^T \\ \boldsymbol{l}_{32} & ({}^{O}\boldsymbol{d_3} \times \boldsymbol{l}_{32})^T \\ \boldsymbol{l}_{36} & ({}^{O}\boldsymbol{d_3} \times \boldsymbol{l}_{33})^T \end{bmatrix}. \quad (15)$$

C. Structural Parameter Optimization of the operator interface

An optimization method is proposed to optimize the kinematic performance and workspace of the operator interface by configuring the length values of l_{i2} and l_{i6}. To measure the operational dexterity throughout the workspace, the global conditioning index (GCI) proposed by Gosselin and Angeles [35] was chosen as the indicator, which can be described as:

$$\begin{cases} \eta_{GCI} = \dfrac{\int_w \frac{1}{k} dw}{\int_w dw} \\ k = \|\boldsymbol{J}\|\|\boldsymbol{J}^{-1}\| = \dfrac{\sigma_{\max}}{\sigma_{\min}}, \\ \boldsymbol{J} = \boldsymbol{J_a}^{-1}\boldsymbol{K_a} \end{cases} \quad (16)$$

where w denotes the workspace of the proposed operator interface, $0 < \eta_{GCI} < 1$. k expresses the condition number, $\sigma_{\max}$ and $\sigma_{\min}$ are the maximum and minimum singular values of the Jacobian matrix $\boldsymbol{J}$, respectively. The condition number can quantitatively reflect the transfer relationship between the input and output motions of the mechanism. When $k = 1$, the corresponding structure is kinematically isotropic, and the motion transfer performance is optimal. The larger the k value is, the mechanism tends to be in a singularity architecture.

The larger value η_{GCI} can yield better dexterity performance. However, GCI represents the average global performance and fails to capture dexterity fluctuation across different workspace areas. To address this issue, the Global Conditioning Mean Square Error Index (GCSEI) is introduced to provide a more comprehensive assessment, which can be described as

$$\eta_{GCSEI} = \sqrt{\frac{\int_w \left(\frac{1}{k} - GCI\right)^2 dw}{\int_w dw}}. \tag{17}$$

A smaller GCSEI corresponds to more excellent stability in dexterity performance. To provide a comprehensive evaluation of the kinematic performance of the operator interface, the mechanism's kinematic performance can be expressed as

$$f_k = \eta_{GCI} - \eta_{GCSEI} \tag{18}$$

A larger value of f_k indicates a superior mechanism's overall kinematic performance.

To optimize the workspace of the haptic operator interface, the linkage length utilization factor has been introduced, which can be described as:

$$f_u = \frac{\sqrt[3]{V}}{l_{i2} + l_{i6}}, \tag{19}$$

where V is the workspace volume of the operator interface. A higher value of f_u indicates more efficient utilization of structural length. Considering the practical application scenario of the operator interface, where both the kinematic characteristics and workspace are essential, the weights of f_k and f_u are set to be the same. Therefore, the overall fitting function can be expressed as

$$f_o = f_k + f_u. \tag{20}$$

Subsequently, the optimization problem can be described as:

$$Z = \mathbf{max}[f_o(\boldsymbol{X})], \boldsymbol{X} = [l_{i2}, l_{i6}]^T$$
$$\boldsymbol{subject\ to} \begin{cases} 50 \le L_2 \le 250\ mm \\ 50 \le L_3 \le 300\ mm \end{cases}, \tag{21}$$

where $\boldsymbol{X}$ denotes a vector representing the structural parameters. The constraint is imposed on the length of l_{i2} and l_{i6} to prevent the excessive size of the operator interface that could negatively impact interaction performance. l_{i2} and l_{i6} are arranged in combinations with a 0.5 mm interval to generate an experimental data set. For each data set, the workflow for the fitness function calculation process is shown in Fig. 3a), and f_o is solved and plotted as illustrated in Fig. 3b). It can be observed that the performance of the operator interface is optimized when $l_{i2} = 145\ \mathrm{mm}$, $l_{i6} = 153\ \mathrm{mm}$, leading to an overall fitness function value of $f_o = 1.6375$.

D. Decoupling Analysis of the Operating Force and Clamping Force

The static force decoupling analysis is conducted to minimize the interference between the clamping feedback force and the 6D spatial feedback force. Subsequently, the motor torque required to output the desired feedback force is calculated based on the Principle of Virtual Work. Fig. 1c) defines the terms and frames for the analysis, where f_i (i=1, 2, 3;) represents forces exerted by each branch chain on the mobile plate. F and M denote the spatial feedback force and torque. f_{ix} and f_{iy} are the two components of f_i on the XY plane, thus f_{3x} denotes the clamping force.

Assuming that the mobile plate is in a state of force equilibrium, the static forces and moment against Point P are related as:

$$\begin{bmatrix} -F_x \\ -F_y \\ -F_z \\ -M_x \\ -M_y \\ -M_z \end{bmatrix} = \begin{bmatrix} f_{1x} + f_{2x} + f_{3x} \\ f_{1y} + f_{2y} + f_{3y} \\ f_{1z} + f_{2z} + f_{3z} \\ f_{1z}y_1 + f_{2z}y_2 + f_{3z}y_3 \\ -f_{2z}x_2 - f_{3z}X_3 \\ -f_{1x}y_1 - f_{2x}y_2 - f_{3x}y_3 + f_{2y}x_2 + f_{3y}X_3 \end{bmatrix}. \tag{22}$$

Combining equations (22-23) and rearranging them in matrix form, there is

$$\begin{bmatrix} f_{1z} \\ f_{2z} \\ f_{3z} \end{bmatrix} = \begin{bmatrix} 1 & 1 & 1 \\ y_1 & y_2 & y_3 \\ 0 & -x_2 & -X_3 \end{bmatrix}^{-1} \begin{bmatrix} -F_z \\ -M_x \\ -M_y \end{bmatrix}. \tag{23}$$

By taking the moments of the components of $\boldsymbol{f_1}, \boldsymbol{f_2}, \boldsymbol{f_3}, \boldsymbol{F}$ and $\boldsymbol{M}$ on the XY plane of the end-effector for the points D_1, D_2, and D_3, respectively, the static force relation can be obtained:

$$\begin{bmatrix} -M_z - F_x y_1 \\ -M_z + F_x y_2 + F_y x_2 \\ -M_z - F_x y_3 + F_y X_3 \end{bmatrix} = $$
$$\begin{bmatrix} f_{2x}(y_1 - y_2) + f_{3x}(y_1 - y_3) + f_{2y}x_2 + f_{3y}X_3 \\ f_{1x}(y_2 - y_1) - f_{1y}x_2 + f_{3y}(X_3 - x_2) \\ f_{1x}(y_3 - y_1) - f_{1y}X_3 + f_{2y}(x_2 - X_3) \end{bmatrix}. \tag{24}$$

Equations (22, 24) can be combined and rearranged in a matrix form as:

$$\boldsymbol{L}\begin{bmatrix} f_{1x} \\ f_{2x} \\ f_{3x} \\ f_{1y} \\ f_{2y} \\ f_{3y} \end{bmatrix} = \begin{bmatrix} -M_z \\ -M_z - F_x y_1 \\ -M_z - F_x y_2 + F_y x_2 \\ -M_z - F_x y_3 + F_y X_3 \\ -F_x \\ -F_y \end{bmatrix}, \tag{25}$$

$$\boldsymbol{L} = \begin{bmatrix} -y_1 & -y_2 & -y_3 & 0 & x_2 & X_3 \\ 0 & y_1 - y_2 & y_1 - y_3 & 0 & x_2 & X_3 \\ y_2 - y_1 & 0 & 0 & -x_2 & 0 & X_3 - x_2 \\ y_3 - y_1 & 0 & 0 & -X_3 & x_2 - X_3 & 0 \\ 1 & 1 & 1 & 0 & 0 & 0 \\ 0 & 0 & 0 & 1 & 1 & 1 \end{bmatrix}. \tag{26}$$

Solving the above equations for the manipulator, its augmented matrix takes the following form.

$$\boldsymbol{M} = \begin{bmatrix} 0 & 0 & 0 & 0 & 0 & 0 & 0 \\ 0 & 0 & 0 & 0 & 0 & 0 & 0 \\ 0 & 0 & 0 & 0 & 0 & 0 & 0 \\ y_3 - y_1 & 0 & 0 & -X_3 & x_2 - X_3 & 0 & M_z - F_x y_3 + F_y x_3 \\ 1 & 1 & 1 & 0 & 0 & 0 & -F_x \\ 0 & 0 & 0 & 1 & 1 & 1 & -F_y \end{bmatrix}. \tag{27}$$

The augmented matrix M is not of full rank, and there are infinite solutions to Equation (25). Therefore, the gripping feedback force $f_{1x} = f_c$ can be set arbitrarily without interfering with the 6D feedback forces provided to the palm, which means that the decoupling between the gripping feedback force and the 6D feedback forces is realized in the static situation. The following is one of the specialized solutions:

$$f_{1x} = f_c, \quad f_{1y} = 0, \quad f_{2y} = f_{3y}. \tag{28}$$

By combining Equations (25,28), the static force solution can be derived as:

$$\begin{bmatrix} f_{1x} \\ f_{2x} \\ f_{3x} \\ f_{1y} \\ f_{2y} \\ f_{3y} \end{bmatrix} = \begin{bmatrix} f_c \\ -F_x - f_{2x} \\ \dfrac{2M_z - 2f_c y_1 - 2F_x y_3 + F_y(x_2+x_3)}{2(y_2 + y_3)} \\ \dfrac{-2M_z + 2f_c y_1 - 2F_x y_2 - F_y(x_2+x_3)}{2(y_2 + y_3)} \\ -\dfrac{F_y}{2} \\ -\dfrac{F_y}{2} \end{bmatrix}. \tag{29}$$

The target torque for each motor is then determined based on the aforementioned target force results. According to the principle of virtual work, the work done in Cartesian terms is equivalent to the work done in joint-space terms.

$$\mathcal{F} \cdot \delta x = \tau \cdot \delta\Theta \tag{30}$$

where $\mathcal{F}$ is a Cartesian force vector acting at the end-effector, δx is an infinitesimal Cartesian displacement of the end-effector, τ s a vector of joint torques, and $\delta\Theta$ is a vector of infinitesimal joint displacement.

The definition of the Jacobian matrix of the ith equivalent 3-DoF serial branch is

$$\delta x = J_{Si} \cdot \delta\Theta, \tag{31}$$

Therefore, Equation (30) can be written as

$$\tau = J_{Si}^T \mathcal{F}. \tag{32}$$

where J_{Si} is derived based on Equation (4) as follows:

$$J_{Si} = \begin{bmatrix} -l_2 s_{\theta_{i1}} c_{\theta_{i2}} - l_3 s_{\theta_{i1}} c_{\theta_{i3}} & -l_2 c_{\theta_{i1}} s_{\theta_{i2}} & -l_3 c_{\theta_{i1}} s_{\theta_{i3}} \\ l_2 c_{\theta_{i1}} s_{\theta_{i2}} + l_3 c_{\theta_{i1}} c_{\theta_{i2}} & -l_2 s_{\theta_{i1}} s_{\theta_{i2}} & -l_3 s_{\theta_{i1}} s_{\theta_{i3}} \\ 0 & l_2 c_{\theta_{i2}} & l_3 c_{\theta_{i3}} \end{bmatrix} \tag{33}$$

By combining Equations (23,29, 32-33), the target torque of each driving motor can be determined.

III. EXPERIMENTS AND RESULTS

A. Hardware Configuration of the Proposed Operator Interface

The proposed operator interface has been prototyped, and the corresponding control hardware configuration has been established, as shown in Fig. 4. The hardware setup mainly consists of a console PC, an embedded central controller, 9 amplifiers, and the operator interface prototype. Nine brushless DC (BLDC) motors (ECG2854, Visan, China) are equipped with the prototype in three groups, each integrating a high-resolution incremental encoder (EN22A) to measure the rotational angle and a planetary gearbox (43.5:1). The binocular vision measurement device (Polaris VEGA ST, NDI, CA) detects the position of the optical marker attached to the mobile plate.

The console PC employs the kinematics algorithm to accurately determine the position of the prototype. Meanwhile, it can process the force sensing data from the RAMIS process and convert it into target feedback output torque for each servo motor. These position and torque data are transferred from the console PC to the embedded central controller (Beckhoff GmbH, Germany) via TCP/IP. The embedded controller generates motion commands later sent via the EtherCAT bus to amplifiers (Uservo-Flex, MotionG, China) for servo control. The amplifier can operate in two modes: cyclic synchronous
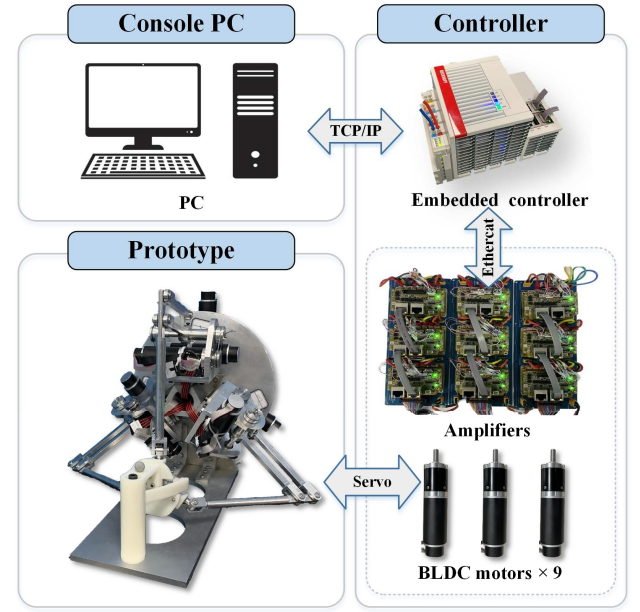

Fig. 4. The hardware configuration of the proposed haptic master manipulator.

torque (CST) and cyclic synchronous position (CSP). The open-loop torque control for the BLDC motors can be achieved by adjusting the current level in the CST mode. The linear relationship between each motor's output torque and current has been calibrated. The semi-closed-loop position servo control can be realized in the CSP mode. The control frequency is set to 1000 Hz to ensure real-time operation.

B. Experiments for the Translational and Orientational Workspace of the Operator Interface

The experimental setup for the valuation of the proposed operator interface's translational and orientational workspace of the proposed operator interface is illustrated in Fig. 5a). Two spherical optical markers were affixed to the handle of the mobile plate. A manual manipulation of the handle was performed by the user, and the corresponding motion trajectories were recorded by the NDI optical tracking unit. The limit translational positions and orientational angles were determined by the recorded data. The achievable translational workspace of the experiments is demonstrated in Fig. 5b). The calculated limit translational range was 315 mm in the X direction, 248.5 mm in the Y direction and 133.8 mm in the Z direction. The limit orientation angle α about the X-axis, angle β about the Y-axis, and γ about the Z-axis in the base frame were shown in the test rig of Fig. 5c). The angle ranges of β and γ can reach up to [-134°, 134°] and [-115°, 115°], respectively. The angles range of α were [-108°, 98°]. The experimental results demonstrate that the proposed operator interface offers an expanded translational workspace and significantly enhanced orientation angles due to the employment of the combined tendon and linkage transmissions. Therefore, the proposed device showcases the potential for integration into RAMIS to match up with diverse configurations of slave manipulators. In addition, it can be observed that the maximum angles of α about the X-axis in the positive direction were
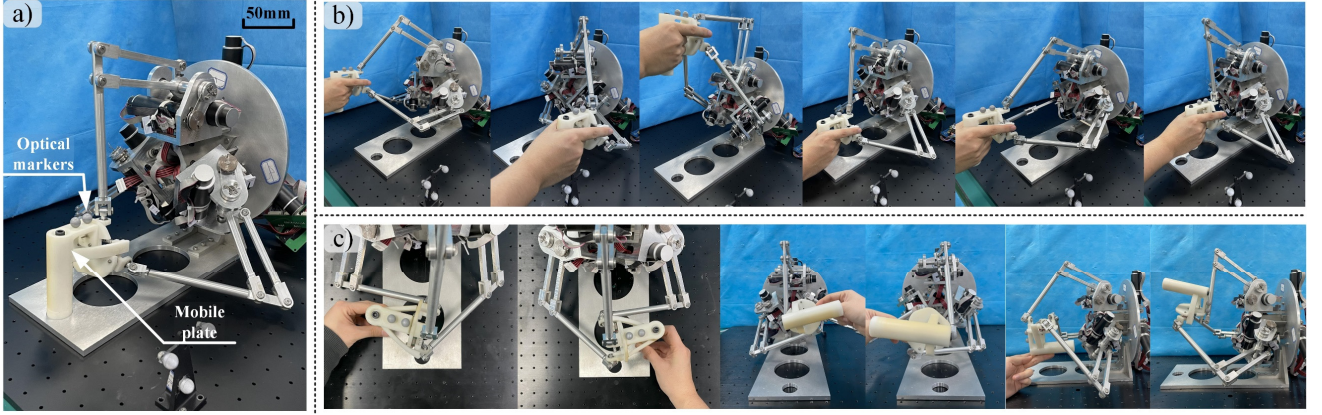
Fig. 5. a) The setup for the investigation of the translational and orientational workspace of the prototype. b) The limited translational position that the user can reach by operating the prototype. c) The maximum achievable orientational angle can reached by the master manipulator.
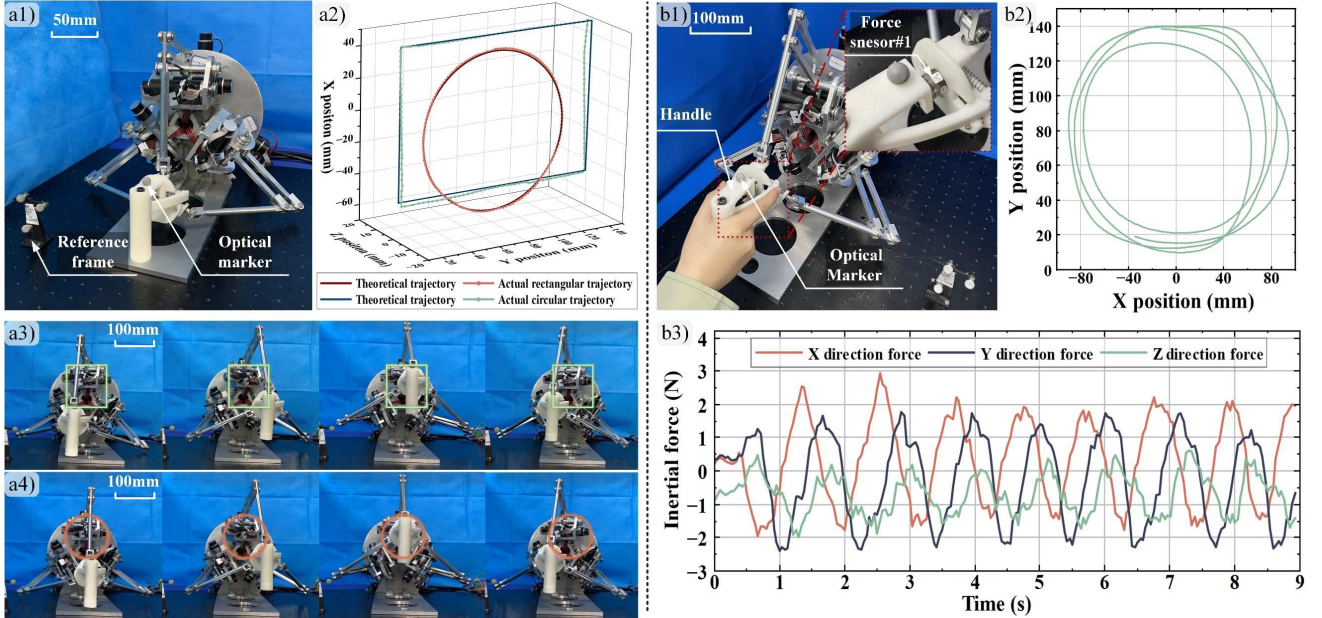

Fig. 6. a1) Experimental setup of the investigation on the positioning accuracy of the prototype. a2) Comparison of the theoretical trajectory and actual trajectory. a3-a4) The actual state of the master manipulator running the rectangular and circular trajectory. b1) The experimental setup of the operational inertia for the master manipulator. b2) The actual motion trajectory of the handle recorded by the NDI optical tracking unit. b3) The actual forces exerted on the handle recorded by the force sensor #1.

smaller than those in the negative direction. This discrepancy can be attributed to the occlusion caused by the horizontal base, and appropriately elevating the support can effectively enhance this orientational angle.

C. Investigation of the Positioning Accuracy of the Operator Interface

The positioning accuracy of the proposed operator interface has been evaluated, and the experimental setup is shown in Fig. 6a1). The amplifiers operated in the CSP mode and the mobile plate of the operator interface was controlled to move along a circular trajectory with a diameter of 100 mm and a rectangular trajectory (100 mm * 140 mm). An optical maker was attached to the mobile plate of the operator interface, and the NDI unit recorded the position. The experimental results are shown in Fig. 6a2-a4). The root mean square error (RMSE) values for the

two experiments were 1.021 mm and 1.223 mm, respectively, demonstrating reasonable positioning accuracy. The result can be attributed to two possible factors. Firstly, there are systematic errors caused by the manufacturing and assembly processes of the prototype. Secondly, there are random errors caused by uncertain factors, such as clearance in the planetary gearbox reducer and environmental noise.

D. Investigation on Inertia Effects of the Operating Handle

The operational inertia of the designed operator interface was investigated with the experimental setup shown in Fig. 6b1). A spherical optical marker was attached to the handle of the prototype. The operational inertia was measured using a high-resolution, multi-dimensional force sensor #1 (NANO 17, ATI Industrial Automation, USA) due to its compactness and capability for precise force measurement in multiple

dimensions. Force sensor #1 was installed between the handle and the mobile plate. All amplifiers were operated in CST mode, and each motor's output torque was set to 0. During the experiment, the operator manually manipulated the handle along a circular trajectory with a diameter of about 150 mm in the XY plane at a speed of approximately 150 mm/s. The motion trajectory of the handle on the mobile plate and the forces exerted were recorded by the NDI optical tracking unit and the force sensor #1, respectively. The experimental results are shown in Fig. 6b2-b3), where it can be observed that the operating forces in the X and Y directions changed periodically with the circular motion of the handle. The maximum forces in the X and Y directions were approximately 3 N and 2.5 N, respectively. The operating force peaked when the operator interface changed the direction between the X and Y directions, indicating that the resistance encountered by the operator during the operation was mainly due to inertial forces. In addition, the average resultant force in the X and Y directions was 1.8 N. This indicates that a small force was required to manipulate the operator interface, effectively reducing fatigue during the long-term operation.

E. Investigation of the Operating Force Output Accuracy

The operating force output accuracy of the haptic operator interface was experimentally investigated. The operating force was experimentally measured using a 6D force sensor #2 (KWR75A, Kunwei Technology, China), which offers a wide range of force measurement capabilities up to 50 N in the X, Y, and Z directions. This sensor was first assembled onto the mobile plate of the operator interface and then fixed onto the distal part of a UR-10 robot arm, as shown in Fig. 7a). The robot arm drove the force sensor and the mobile plate of the operator interface to reach five discrete positions, and the corresponding coordinates of these positions are shown in Table III.

TABLE III
COORDINATES OF THE EXPERIMENTAL POINTS OF FORCE SENSOR

	Coordinate(mm)
Point 1	(0, 0, 205)
Point 2	(-85, -40, 185)
Point 3	(85, -40, 185)
Point 4	(85, 40, 185)
Point 5	(-85, 40, 185)

The target output forces of the operator interface were set from 0 to 8 N with an increment of 1 N in the X, Y, and Z directions, respectively. Then, the target torque of each driving motor was determined by the equations specified in *Section II.D.* The amplifiers operated in the CST mode, sending commands to each motor. The corresponding force sensor data at the five positions were recorded and averaged, as shown in Fig. 7b). The average errors of output force in the three directions were 0.084 N, 0.124 N, and 0.237 N, respectively. These experimental results indicate that the proposed operator interface generates high accuracy in operating force output. In addition, it can be observed that the output force error in the Z direction was slightly larger than that in the X and Y directions. This happens because more motors are required to work and output torque for the Z direction, resulting in the accumulation
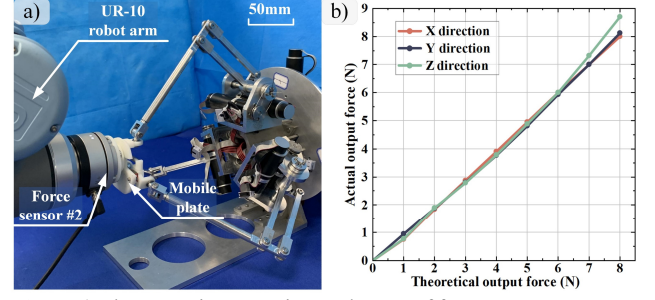
of motor torque output errors.

Fig. 7. a) The operating experimental setup of force output accuracy for the master manipulator. b) Comparison of the theoretical output force and actual operating output force within 0-8 N.

F. Validation of Force Decoupling Capability of the Operation Force and Clamping Force
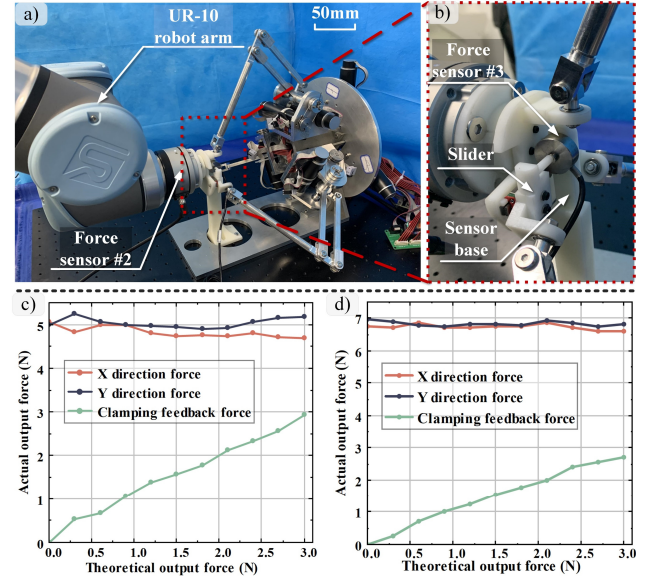

Fig. 8. a) The experimental setup of force decoupling capability for the master manipulator. b) Arrangement of sensor #3 to measure the clamping force. c-d) The measured forces in the X and Y directions, as well as the clamping force recorded by the two sensors.

The experimental setup for the decoupling capability investigation of the 6D operating force and 1D clamping force of the designed operator interface is shown in Fig. 8a-b). Force sensor #2 was fixed onto the UR-10 robot arm to measure the operating output force of the operator interface arm. Force sensor #3 (Jinnuo, JHBM-M2, China) was chosen to measure the clamping feedback force, which measures only 1D force and has an ultra-thin profile of just 10 mm. The amplifiers operated in the CST mode, and the mobile plate outputted 5 N and 7 N forces in the X and Y directions, respectively. Then, the slider outputted the clamping force progressively from 0 N to 3 N with a 0.3 N increment, and the data from two force sensors was recorded. The experimental results are shown in Fig. 8c-d). As the output clamping force increased, there was a slight fluctuation in the operating force for the operator interface ends in the X and Y directions. The fluctuation range

TABLE IV
COMPARISON OF THE PROPOSED INTERFACE WITH THE EXISTING STATE-OF-THE-ART DEVICE

Device	Structure	Translational workspace (mm^3)	Rotational workspace (°)	DoFs	Force	Inertia	Refresh rate
Sigma. 7	"Delta" and serial	$\phi190 \times 130$	$235 \times 140 \times 200$	7	20N	Heavy	Up to 4k Hz
Phantom	Full serial	$431 \times 348 \times 165$	-	6	3.3N	Light	Up to 1k Hz
Omega. 3	"Delta"	$\phi160 \times 110$	-	3	12N	Medium	Up to 4k Hz
Ours	Redundant parallel	$315 \times 249 \times 134$	$268 \times 230 \times 206$	7	8N	Light	Up to 10k Hz

was 0.37 N and 0.27 N, accounting for 7.4% (operating force 5 N) and 3.8% (operating force 7 N), respectively. In addition, the average output errors of the clamping force were 0.095 N and 0.081 N, respectively. The experimental results demonstrated that the proposed operator interface exhibited high accuracy in clamping force output. In addition, the utilization of the decoupling force output strategy ensures minimal interference between the operating force and the gripping force.

IV. DISCUSSION

A novel 7-DOF haptic device is proposed and prototyped, featuring a redundantly actuated configuration that effectively circumvents workspace-interior singularities. As a result, it achieves an expansive translational workspace measuring 315 mm (X), 248.5 mm (Y), and 133.8 mm (Z), accompanied by a wide range of orientation angles [-108°, 98°] (α), [-134°, 134°] (β) and [-115°, 115°] (γ). The 3-DoF full actuation of each branch chain is achieved by the introduced redundancy, allowing the proximal actuation of the clamping DoF. Additionally, the motor arrangement has been specially designed to be near the base, which effectively reduces the operating inertia force (averaging 1.8 N) and fatigue during RAMIS surgery. Static force decoupling analysis was performed, allowing the interference between the clamping feedback force and the 6D spatial feedback force to be minimized, which has been demonstrated by the experimental results. To further improve the positioning accuracy of the proposed robot, a specifically designed calibration procedure will be developed to reduce the system error. In addition, random errors can be further reduced by replacing the gap-free motors, replacing more accurate measurement equipment, and increasing the number of experiments to average. The technical capabilities and performances of this interface and other existing state-of-the-art devices have been summarized in Table IV. Compared with the commercial haptic interface, this device has significant advantages in translational and rotational workspace, DoFs, operational inertia, and refresh rate. However, the force output performance and position resolution need to be improved. Moreover, the translational motion range in the Z direction is limited compared with that in other directions, which can be addressed by optimizing the placement of the motors away from the mobile plate and enlarging the overall size of linkages.

V. CONCLUSION

This paper proposes a novel operator interface that can address the problem of the difficult trade-off between workspace and operational stiffness in the application of traditional series and parallel devices on the RAMIS process by introducing the redundantly actuated parallel structure. Both tendon and linkage transmissions are employed to avoid the backlash error and enhance structural compactness. A structure parameter optimization method is proposed to optimize the kinematic performance and workspace of the operator interface. The operator interface has been prototyped, and experiments have been conducted to validate its performance. The experimental results demonstrated that the proposed operator interface generates high accuracy in operating force output, exhibits high accuracy in clamping force output, and has effective decoupling capability between the operating and gripping forces. The positioning accuracy and inertia experiments have been evaluated, demonstrating that the proposed operator interface can exhibit reasonable positioning accuracy, and a small force is required to manipulate this device to reduce operational fatigue. Moreover, the proposed redundantly actuated parallel structure can be further applied to developing general haptic devices. Future work will focus on friction compensation [36], [37] and control scheme development [31], [38], [39] to enhance the operational performance during operation.

REFERENCES

[1] P. E. Dupont, B. J. Nelson, M. Goldfarb, *et al.*, "A decade retrospective of medical robotics research from 2010 to 2020," *Sci. Robot.*, vol. 6, no. 60, p. eabi8017, Nov. 2021, doi: 10.1126/scirobotics.abi8017.

[2] J. Li, S. Wang, Z. Zhang, *et al.*, "A Robotic System for Transanal Endoscopic Microsurgery: Design, Dexterity Optimization, and Prototyping," *IEEE Robot. Autom. Mag.*, pp. 2–16, 2023, doi: 10.1109/MRA.2023.3323849.

[3] T. Haidegger, S. Speidel, D. Stoyanov, *et al.*, "Robot-Assisted Minimally Invasive Surgery—Surgical Robotics in the Data Age," *Proc. IEEE*, vol. 110, no. 7, pp. 835–846, Jul. 2022, doi: 10.1109/JPROC.2022.3180350.

[4] D. Song, S. Wang, Z. Zhang, *et al.*, "A Novel Continuum Overtube With Improved Triangulation for Flexible Robotic Endoscopy," *IEEE Trans. Med. Robot. Bionics*, vol. 5, no. 3, pp. 657–668, Aug. 2023, doi: 10.1109/TMRB.2023.3294527.

[5] V. Vitiello, S.-L. Lee, T. P. Cundy, *et al.*, "Emerging robotic platforms for minimally invasive surgery," *IEEE Rev. Biomed. Eng.*, vol. 6, pp. 111–126, 2013, doi: 10.1109/RBME.2012.2236311.

[6] Z. Lin, Z. Xu, H. Liu, *et al.*, "Robotic Manipulator-Assisted Omnidirectional Augmented Reality for Endoluminal Intervention Telepresence," *Adv. Intell. Syst.*, vol. n/a, no. n/a, p. 2300373, doi: 10.1002/aisy.202300373.

[7] X. Luo, D. Song, Z. Zhang, *et al.*, "A Novel Distal Hybrid Pneumatic/Cable-Driven Continuum Joint with Variable Stiffness Capacity for Flexible Gastrointestinal Endoscopy," *Adv. Intell. Syst.*, vol. 5, no. 6, p. 2200403, Jun. 2023, doi: 10.1002/aisy.202200403.

[8] C.-H. Kuo and J. S. Dai, "Robotics for Minimally Invasive Surgery: A Historical Review from the Perspective of Kinematics," in *International Symposium on History of Machines and Mechanisms*, H.-S. Yan and M. Ceccarelli, Eds., Dordrecht: Springer Netherlands, 2009, pp. 337–354. doi: 10.1007/978-1-4020-9485-9_24.

[9] D. Wu, J. Li, D. Song, *et al.*, "Development of a Novel Ball-and-Socket Flexible Manipulator for Minimally Invasive Flexible Surgery," *IEEE Trans. Med. Robot. Bionics*, vol. 5, no. 2, pp. 278–288, May 2023, doi: 10.1109/TMRB.2023.3265714.

[10] P. Gomes, "Surgical robotics: Reviewing the past, analysing the present, imagining the future," *Robot. Comput.-Integr. Manuf.*, vol. 27, no. 2, pp. 261–266, Apr. 2011, doi: 10.1016/j.rcim.2010.06.009.

[11] J. Zhu, L. Lyu, Y. Xu, *et al.*, "Intelligent Soft Surgical Robots for Next-Generation Minimally Invasive Surgery," *Adv. Intell. Syst.*, vol. 3, no. 5, p. 2100011, 2021, doi: 10.1002/aisy.202100011.

[12] Y. Xu, D. Song, Z. Zhang, *et al.*, "A Novel Extensible Continuum Robot with Growing Motion Capability Inspired by Plant Growth for Path-Following in Transoral Laryngeal Surgery," *Soft Robot.*, vol. 11, no. 1, pp. 171–182, Feb. 2024, doi: 10.1089/soro.2023.0014.

[13] J. A. Saglia, J. S. Dai, and D. G. Caldwell, "Geometry and Kinematic Analysis of a Redundantly Actuated Parallel Mechanism That Eliminates Singularities and Improves Dexterity," *J. Mech. Des.*, vol. 130, no. 124501, Oct. 2008, doi: 10.1115/1.2988472.

[14] M. Sreelakshmi and T. D. Subash, "Haptic Technology: A comprehensive review on its applications and future prospects," *Mater. Today Proc.*, vol. 4, no. 2, Part B, pp. 4182–4187, Jan. 2017, doi: 10.1016/j.matpr.2017.02.120.

[15] A. Talvas, M. Marchal, and A. Lécuyer, "A Survey on Bimanual Haptic Interaction," *IEEE Trans. Haptics*, vol. 7, no. 3, pp. 285–300, Jul. 2014, doi: 10.1109/TOH.2014.2314456.

[16] J. Zhao, J. Li, L. Cui, *et al.*, "Design and performance investigation of a robot-assisted flexible ureteroscopy system," *Appl. Bionics Biomech.*, vol. 2021, 2021, doi: 10.1155/2021/6911202.

[17] C. Freschi, V. Ferrari, F. Melfi, *et al.*, "Technical review of the da Vinci surgical telemanipulator," *Int. J. Med. Robot.*, vol. 9, no. 4, pp. 396–406, 2013, doi: 10.1002/rcs.1468.

[18] G. H. Ballantyne and F. Moll, "The da Vinci telerobotic surgical system: the virtual operative field and telepresence surgery," *Surg. Clin. North Am.*, vol. 83, no. 6, Art. no. 6, Dec. 2003, doi: 10.1016/S0039-6109(03)00164-6.

[19] H. Sang, S. Wang, J. Li, *et al.*, "Control design and implementation of a novel master–slave surgery robot system, MicroHand A," *Int. J. Med. Robot.*, vol. 7, no. 3, Art. no. 3, 2011, doi: 10.1002/rcs.403.

[20] Y. Liang, L. Sun, Z. Du, *et al.*, "Mechanism design and optimization of a haptic master manipulator for laparoscopic surgical robots," *IEEE Access*, vol. 7, pp. 147808–147824, 2019, doi: 10/gswsdz.

[21] M. Hwang and D.-S. Kwon, "K-FLEX: A flexible robotic platform for scar-free endoscopic surgery," *Int. J. Med. Robot.*, vol. 16, no. 2, p. e2078, 2020, doi: 10.1002/rcs.2078.

[22] A. J. Silva, O. A. D. Ramirez, V. P. Vega, *et al.*, "PHANToM OMNI Haptic Device: Kinematic and Manipulability," in *2009 Electronics, Robotics and Automotive Mechanics Conference (CERMA)*, Sep. 2009, pp. 193–198. doi: 10.1109/CERMA.2009.55.

[23] D. Ji, S. Shim, S. Kim, *et al.*, "Master device with bending safety for flexible surgical robots," *J. Mech. Robot.-Trans. Asme*, vol. 12, no. 6, Art. no. 6, 2020, doi: 10.1115/1.4046996.

[24] M. H. Vu and U. J. Na, "A new 6-DOF haptic device for teleoperation of 6-DOF serial robots," *IEEE Trans. Instrum. Meas.*, vol. 60, no. 11, Art. no. 11, 2011, doi: 10.1109/TIM.2011.2164285.

[25] H. Shen, C. Wang, L. Xie, *et al.*, "A novel remote-controlled robotic system for cerebrovascular intervention," *Int. J. Med. Robot.*, vol. 14, no. 6, p. e1943, 2018, doi: 10.1002/rcs.1943.

[26] U. Hagn, R. Konietschke, A. Tobergte, *et al.*, "DLR MiroSurge: a versatile system for research in endoscopic telesurgery," *Int. J. Comput. Assist. Radiol. Surg.*, vol. 5, no. 2, pp. 183–193, Mar. 2010, doi: 10.1007/s11548-009-0372-4.

[27] A. Tobergte, P. Helmer, U. Hagn, *et al.*, "The sigma.7 haptic interface for MiroSurge: A new bi-manual surgical console," in *2011 IEEE/RSJ International Conference on Intelligent Robots and Systems*, Sep. 2011, pp. 3023–3030. doi: 10.1109/IROS.2011.6094433.

[28] Y. Chen, C. Zhang, Z. Wu, *et al.*, "The SHURUI System: A Modular Continuum Surgical Robotic Platform for Multiport, Hybrid-Port, and Single-Port Procedures," *IEEEASME Trans. Mechatron.*, pp. 1–12, 2021, doi: 10/gm6mn3.

[29] J. Shang, K. Leibrandt, P. Giataganas, *et al.*, "A Single-Port Robotic System for Transanal Microsurgery—Design and Validation," *IEEE Robot. Autom. Lett.*, vol. 2, no. 3, Art. no. 3, 2017, doi: 10.1109/LRA.2017.2668461.

[30] C. Kuo, J. S. Dai, and P. Dasgupta, "Kinematic design considerations for minimally invasive surgical robots: an overview," *Int. J. Med. Robot.*, vol. 8, no. 2, pp. 127–145, Jun. 2012, doi: 10.1002/rcs.453.

[31] J. A. Saglia, N. G. Tsagarakis, J. S. Dai, *et al.*, "A High-performance Redundantly Actuated Parallel Mechanism for Ankle Rehabilitation," *Int. J. Robot. Res.*, vol. 28, no. 9, pp. 1216–1227, Sep. 2009, doi: 10.1177/0278364909104221.

[32] C. Gosselin and L.-T. Schreiber, "Kinematically Redundant Spatial Parallel Mechanisms for Singularity Avoidance and Large Orientational Workspace," *IEEE Trans. Robot.*, vol. 32, no. 2, pp. 286–300, Apr. 2016, doi: 10.1109/TRO.2016.2516025.

[33] C. Gosselin and L.-T. Schreiber, "Redundancy in parallel mechanisms: A review," *Appl. Mech. Rev.*, vol. 70, no. 1, p. 010802, 2018, doi: 10.1115/1.4038931.

[34] C. Gosselin, T. Laliberté, and A. Veillette, "Singularity-Free Kinematically Redundant Planar Parallel Mechanisms With Unlimited Rotational Capability," *IEEE Trans. Robot.*, vol. 31, no. 2, pp. 457–467, Apr. 2015, doi: 10.1109/TRO.2015.2409433.

[35] J. Angeles, "The Design of Isotropic Manipulator Architectures in the Presence of Redundancies," *Int. J. Robot. Res.*, vol. 11, no. 3, pp. 196–201, Jun. 1992, doi: 10.1177/027836499201100303.

[36] A. Dong, Z. Du, and Z. Yan, "Friction modeling and compensation for haptic master manipulator based on deep Gaussian process," *Mech. Mach. Theory*, vol. 166, p. 104480, Dec. 2021, doi: 10.1016/j.mechmachtheory.2021.104480.

[37] J. Yao, W. Deng, and Z. Jiao, "Adaptive Control of Hydraulic Actuators With LuGre Model-Based Friction Compensation," *IEEE Trans. Ind. Electron.*, vol. 62, no. 10, pp. 6469–6477, Oct. 2015, doi: 10.1109/TIE.2015.2423660.

[38] M. Li, R. Kang, D. T. Branson, *et al.*, "Model-Free Control for Continuum Robots Based on an Adaptive Kalman Filter," *IEEEASME Trans. Mechatron.*, vol. 23, no. 1, pp. 286–297, Feb. 2018, doi: 10.1109/TMECH.2017.2775663.

[39] S. Saini, M. F. Orlando, and P. M. Pathak, "Adaptive Control of a Master-Slave Based Robotic Surgical System With Haptic Feedback," *IEEE Trans. Autom. Sci. Eng.*, pp. 1–0, 2022, doi: 10/gqpxzn.